Physica D 457 (2024) 133942

Contents lists available at ScienceDirect

Physica D

journal homepage: www.elsevier.com/locate/physd

Optimal boundary control of a model thin-film fiber coating model

Shiba Biswal [a,*,1], Hangjie Ji [b,2], Karthik Elamvazhuthi [c], Andrea L. Bertozzi [d]

[a] University of California, Department of Mathematics, Los Angeles, 90095, CA, USA
[b] North Carolina State University, Department of Mathematics, Raleigh, 27695, NC, USA
[c] University of California, Department of Mechanical Engineering, Riverside, 92521, CA, USA
[d] University of California, Department of Mathematics and Mechanical and Aerospace Engineering, Los Angeles, 90095, CA, USA

ARTICLE INFO

Dataset link: https://github.com/ShibaBiswal/Optimal-Boundary-Control-for-Thin-Film-Equation-

Keywords:
Thin-film equation
Optimal control
Boundary control
PDE control
Distributed parameter systems

ABSTRACT

This paper considers the control of fluid on a solid vertical fiber, where the fiber radius is larger than the film thickness. The fluid dynamics is governed by a fourth-order partial differential equation (PDE) that models this flow regime. Fiber coating is affected by the Rayleigh–Plateau instability that leads to breakup into moving droplets. In this work, we show that control of the film profile can be achieved by dynamically altering the input flux to the fluid system that appears as a boundary condition of the PDE. We use the optimal control methodology to compute the control function. This method entails solving a minimization of a given cost function over a time horizon. We formally derive the optimal control conditions, and numerically verify that subject to the domain length constraint, the thin film equation can be controlled to generate a desired film profile with a single point of actuation. Specifically, we show that the system can be driven to both constant film profiles and traveling waves of certain speeds.

1. Introduction

Thin viscous liquid films flowing down vertical cylindrical fibers exhibit complex and interesting interfacial dynamics. Driven by the Rayleigh–Plateau instability, the liquid films form droplets or pulses that flow down along the fiber. The flow dynamics depend on the flow rate, fiber radius, liquid properties, and inlet conditions [1]. These factors can lead to stable trains of droplets that behave like a traveling wave, droplet coalescence, and isolated moving droplets separated by small amplitude waves [2,3]. For applications of such coating flows in particle capture [4], desalination [5,6], and other mass and heat exchangers [7,8], it is crucial to maintain a stable film profile with desired characteristics.

Classical lubrication theory is widely studied for thin liquid films flowing down vertical fibers at small flow rates. In the thin film limit where the characteristic liquid film thickness is significantly smaller than the fiber radius, the leading-order evolution equation for the film thickness h, derived by Trifonov [9] and Frenkel [10], and further studied by [11,12], is given by

$$h_t + \left[\delta h^3 \left(h_x + h_{xxx}\right) + \tfrac{2}{3}h^3\right]_x = 0. \tag{1}$$

Here, $\delta = 2l_c^2 h_0/(3R^3)$ measures the ratio of curvature-driven flow to the gravity driven mean flow, where $l_c = (\sigma/\rho g)^{1/2}$ is the capillary wave length, ρ is the fluid density, g is the gravitational acceleration, σ is the surface tension, and h_0 is the thickness of the initial flat film that is taken to be the characteristic film height. The higher-order term h_{xxx} corresponds to the stabilizing streamwise surface tension, h_x represents the destabilizing azimuthal curvature, and the last term $\frac{2}{3}h^3$ represents gravity. We note that Eq. (1) is a simplified fiber coating model that contains linearized curvatures terms and neglects the geometric contribution of the substrate. More classical models for fiber coating dynamics that incorporate substrate geometry, slip length, moderate inertia and fully-nonlinear curvatures have been developed and investigated in [1,2,13–16].

Introducing a change of scaling $t \to t/\delta$ to Eq. (1) leads to an equivalent model for the film thickness $h(t,x)$ over a domain $0 \le x \le L$,

$$h_t + \left[h^3\left(G + h_x + h_{xxx}\right)\right]_x = 0, \tag{2}$$

where the Bond number $G = 2/(3\delta) = (\rho g R^3)/(\sigma h_0)$. This is a nonlinear fourth-order parabolic type partial differential equation, where h^3 represents the mobility function, and the Bond number G plays a significant role in the solution dynamics. Based on the analysis

* Corresponding author.
E-mail addresses: sbiswal@math.ucla.edu (S. Biswal), hangjie_ji@ncsu.edu (H. Ji), kelamvazhuthi@engr.ucr.edu (K. Elamvazhuthi), bertozzi@math.ucla.edu (A.L. Bertozzi).

[1] SB and AB was supported by Simons Math + X Investigator Award number 510776.
[2] HJ was supported by NSF DMS 2309774.

https://doi.org/10.1016/j.physd.2023.133942
Received 16 May 2023; Received in revised form 24 August 2023; Accepted 2 October 2023
Available online 6 October 2023

in [11,12], given the (initial) average film thickness $h_0 = 1$, traveling pulses that move steadily at constant speeds exist for G smaller than a critical $G_* \approx 0.6$. More recently, Halpern and Wei also investigated slip-enhanced drop formation [17] using a variant of Eq. (2) that incorporates the Navier-slip condition.

In this paper, we aim to control the coating film solution profiles in (2) by controlling the inlet flux at $x = 0$, $q(t, 0)$, where the flux is given by,

$$q(t, x) = h^3(G + h_x + h_{xxx}). \tag{3}$$

This is motivated by recent experimental and analytical studies [1,18] that reveal the importance of the inlet geometry and flow rate to the downstream droplet dynamics. Interesting experimental work for the nonlinear response of the fiber coating dynamics to periodic forcing at the inlet has also been presented in [19]. The authors showed that the spatial response of the downstream dynamics strongly depends on the ratio of the forcing frequency to a critical frequency corresponding to the maximum linear growth rate. Following the work in [1,20], we impose the following Dirichlet boundary conditions $h(t, 0) = h_{in}, q(t, 0) = u(t)$ at the inlet, where the inlet flux $q(t, 0)$ appears as a boundary condition of the PDE that governs the evolution of the film thickness. At the outlet $x = L$, we impose the Neumann boundary conditions $h_x(t, L) = h_{xxx}(t, L) = 0$. We show via numerical studies that Eq. (2) can be controlled to maintain nearly-constant film thickness and desired traveling waves, subject to constraints.

Expanding Eq. (2) around a flat film state, $h(t, x) \sim 1 + \hat{h}(t, x)$, where $\hat{h}(t, x) \ll 1$, we obtain a weakly nonlinear equation,

$$\hat{h}_t + 3G\hat{h}_x + 6G\hat{h}\hat{h}_x + \hat{h}_{xx} + \hat{h}_{xxxx} = 0.$$

Using the rescaling $\hat{h} \to (6G)^{-1}\hat{h}$ and a change of coordinates $x \to x - 3Gt$ in the moving reference frame, this equation can be transformed to the classical Kuramoto–Sivashinsky (KS) equation [12],

$$\hat{h}_t + \hat{h}\hat{h}_x + \hat{h}_{xx} + \hat{h}_{xxxx} = 0. \tag{4}$$

A significant amount of research exists on the control of the KS equation (4). A well-studied approach to controlling this PDE is to obtain a finite-dimensional approximation a reduced-order-model (ROM) that captures the dominant dynamics of the PDE, and then apply standard control methodologies to this ROM. For example, some earlier works proposed a distributed control (one that acts on the whole domain) for the KS equation under periodic boundary conditions [21–23]. Another approach to controlling the KS equation is through its boundary term, either the Neumann boundary condition, or the Dirichlet boundary condition. For example, in [24] the linear KS equation is reduced to an equivalent finite dimensional system using the Sturm–Liouville decomposition, and then controlled through its boundary. However, unlike ordinary differential equations, in the case of PDEs, local linear stability may not necessarily imply local nonlinear stability. In the case of KS equation, conditions that guarantee this implication are provided in [25]. A few researchers [26–28] have also shown boundary control of nonlinear KS equation which does not rely on discretization of the PDE is possible. Optimal control of the KS equation is studied in [29]. The literature on control of the full nonlinear thin-film equation, of the type that we consider in this paper, is very limited. In [30], the authors consider an optimal control of a thin-film type equation that only contains the fourth-order derivative. In [31], for a thin film evolving on a plane without any gravitational effect, a linear proportional control for the suppression of the Marangoni instability has been explored. To the best of our knowledge, control of the thin film equation (2) that we consider in this paper has not been studied.

The paper is organized as follows. In Section 2 we formulate the optimal control problem. The details of the derivation are provided in Appendix. We verify the algorithm via numerical simulations presented in Section 3. Section 4 shows concluding remarks of this paper.

2. Optimal control formulation

In this section we introduce and formulate the optimal control problem. We begin by defining the notations, and restating the thin-film equation (2) with its imposed boundary conditions.

We denote the non-dimensional fiber length by L. The state space is denoted by $\Omega = [0, L]$. The symbol $\partial\Omega$ stands for the boundary of Ω. At any given time t and $x \in \Omega$, we let $h(t, x)$ denote the fluid thickness across the fiber length. The flux, denoted by q, is given by (3). In this paper, we set the input flux $q(t, 0)$ to be the time-dependent scalar-valued control parameter $u(t)$.

Consider the one-dimensional PDE (2) again now with its boundary and initial conditions. The system evolves on $[0, T] \times \Omega$.

$$h_t + \left(h^3(G + h_x + h_{xxx})\right)_x = 0$$
$$q(t, 0) = \left(h^3(G + h_x + h_{xxx})\right)\Big|_{(x=0)} = u(t), \tag{5}$$
$$h(t, 0) = h_{in}, \qquad h_x(t, L) = 0, \qquad h_{xxx}(t, L) = 0 \tag{6}$$
$$h(0, x) = h_0 \tag{7}$$

Here, $h_{in} > 0$ is a fixed scalar.

Our goal is to design a $u(t)$ such that the film profile $h(t, x)$ is close to a desired fluid profile $h^d(t, x)$ in the $L^2([0, T], \Omega)$ sense, in a given finite time $T \in (0, \infty)$. Because we have chosen a finite time horizon, this choice of control methodology is called the finite-horizon optimal control problem. In this work, we consider h^d to be both a film of constant thickness and a traveling wave. In the case of traveling wave profiles h^d, we use the periodic boundary condition as opposed to the one outlined above in (5)–(6), the details are provided in Section 3.2. Furthermore, we require that the $(L^2([0, T]))$ norm of control $u(t)$ to be bounded. Therefore, we consider the following objective function,

$$J(h, u) = \frac{1}{2}\int_0^T \|h(t, x) - h^d(t, x)\|^2_{L^2(\Omega)}\, dt + \frac{\lambda}{2}\|u(t)\|^2_{L^2([0,T])}. \tag{8}$$

Here, $\lambda > 0$ is a weighting parameter of choice.

The optimal control problem is posed as a constrained minimization problem of the cost function (8) over a set of controls $U = \{u(t) : 0 \le u(t) \le u_p\}$, subject to the PDE (2) and its boundary conditions defined by Equations (6). Here, u_p is an upper bound on the control. The lower bound is zero, since the control function is the input flux, which is necessarily non-negative. Therefore, the optimal control problem can be stated as follows:

Problem 2.1.

$$\min_{u\in U} J(h, u) = \frac{1}{2}\int_0^T \|h(t, x) - h^d(t, x)\|^2_{L^2(\Omega)}\, dt + \frac{\lambda}{2}\|u(t)\|^2_{L^2([0,T])} \tag{9}$$

subject to,

$$h_t + (h^3(G + h_x + h_{xxx}))_x = 0 \text{ in } [0, T] \times \Omega$$
$$(h^3(G + h_x + h_{xxx}))\Big|_{(x=0)} - u(t) = 0,$$
$$h(t, 0) - h_{in} = 0, \qquad h_x(t, L) = 0, \qquad h_{xxx}(t, L) = 0$$
$$h(0, x) = h_0$$

and

$$0 \le u(t) \le u_p \text{ for a.e. } t.$$

We will use *gradient descent* to find a solution to the optimization problem. However, we note that the cost function (8) is a function of two variables h and u. However, algorithmically, gradient descent is difficult to implement for this optimization problem due to the PDE constraints. To get around this problem, it is standard in the optimal control literature to treat h as a variable dependent on u via the PDE constraint (5). This will enable us to perform gradient descent on the variable u rather than both h and u. Towards this goal, we define the *reduced objective functional* $f : U \to \mathbb{R}$ by $f(u) = J(h(u), u)$ for all $u \in U$,

where $h(u)$ is the solution of the Eqs. (2)–(7) for a given u. In terms of the reduced objective functional, the optimal control Problem 2.1 can alternatively expressed as

Problem 2.2.

$$\inf_{u\in U} f(u)$$

While one can compute the gradient of the function $f(u)$, with respect to u, using the finite difference method, this approach is not numerically tractable since $u(t)$ is a function. Alternatively, one can compute the gradient of $f(u)$ using the *formal Lagrange method* [32] or the method of Lagrange multipliers to the optimization Problem 2.1. This method leads to a numerically tractable expression for this gradient using the so called *adjoint equation*. While the method leads to the formulation of the correct expression for the gradient, the derivation of the conditions is not mathematically rigorous. This is because applying this method to optimization problems with PDE constraints requires addressing additional technicalities, such as the existence of solutions and the differentiability of the objective functional. These technicalities are outside the scope of this paper. We will use the method formally to derive the first order necessary conditions of optimality and provide numerical evidence that this thin film equation can be controlled for certain short lengths using an optimal control approach.

We will now eliminate the constraints by means of Lagrange multipliers, $p_1(t,x)$, $p_2(t)$, $p_3(t)$, $p_4(t)$, $p_5(t)$. The multipliers are grouped into a vector $p = [p_1, p_2, p_3, p_4, p_5]$. The Lagrangian function is defined as follows

$$\begin{aligned}\mathcal{L}(h,u,p) = J(h,u) &- \int_0^T \int_\Omega p_1(t,x)\left(h_t + \left(h^3(G + h_x + h_{xxx})\right)_x\right) dx\, dt \\ &- \int_0^T p_2(t)\left((h^3(G + h_x + h_{xxx}))|_{(x=0)} - u(t)\right) dt \\ &- \int_0^T p_3(t)(h(t,0) - h_{in})dt - \int_0^T p_4(t)h_x(t,L)dt \\ &- \int_0^T p_5(t)h_{xxx}(t,L)dt.\end{aligned}$$

Let $\bar{h}, \bar{u}$ denote the optimal values of $h(t,x)$ and $u(t)$ respectively. Moreover, we will assume that $\bar{h}$ is strictly positive on $[0, L]$; as will be seen later in the Appendix, this assumption will prove to be vital in deriving the optimality conditions. First-order necessary condition requires that the derivative of $\mathcal{L}$ with respect to h must vanish at the optimal point $(\bar{h}, \bar{u})$, that is,

$$D_h\mathcal{L}(\bar{h}, \bar{u}, p)v = 0,\ \forall v \text{ s.t. } v(0,x) = 0. \tag{10}$$

The condition $v(0,x) = 0$ imposed on the perturbation v ensures that the initial condition (7) is fixed. This necessary condition yields the following adjoint equation and the corresponding boundary conditions. Details of the derivation have been provided in the Appendix.

$$\begin{aligned}-(p_1)_t = (\bar{h} - h^d) + (p_1)_x(3\bar{h}^2(G + \bar{h}_x + \bar{h}_{xxx})) - \left((p_1)_x\bar{h}^3\right)_x \\ - \left((p_1)_x\bar{h}^3\right)_{xxx} \text{ in } \Omega\end{aligned} \tag{11}$$

$$(p_1)_x(t,0) = 0, \tag{12}$$

$$(p_1)_{xx}(t,0) = 0 \tag{13}$$

$$(p_1)_x(t,L) = 0 \tag{14}$$

$$-p_1(t,L) + (p_1)_{xxx}(t,L) = 0 \tag{15}$$

$$p_1(T,x) = 0 \tag{16}$$

The adjoint equation is solved backward in time, therefore the final-time condition (16) is the initial condition for the adjoint equation. The initial condition set to zero here as per Eq. (33) (in Appendix).

The gradient of the reduced objective functional $f(u)$ with respect to u can be computed using the gradient of the Lagrangian [32] as

$$f_u(u) = D_u\mathcal{L}(h,u,p). \tag{17}$$

From the constraints on u, we deduce that the optimal control $\bar{u}$ must satisfy the following variational inequality,

$$D_u\mathcal{L}(\bar{h}, \bar{u}, p)(u - \bar{u}) = \int_0^T (\lambda\bar{u} + \bar{p}_2)(u - \bar{u}) \geq 0,\ \forall u \in U \tag{18}$$

To find $(\bar{h}, \bar{u})$, we perform gradient descent on the optimization problem using the expression for the gradient in (17). The system (2)–(6) is solved forward in time $t \in [0,T]$, hence it is called the *forward equation*. As previously mentioned, the adjoint Eq. (11)–(15) is solved backward in time $\tau = T - t \in [0,T]$, hence it is referred to as the *backward equation*. The search for an optimal control entails performing a gradient descent on u. The algorithm is presented in Algorithm 1. Statements 9–11 in Algorithm 1 implement the *projected gradient method* [33]. This ensures that the obtained u is strictly non-negative. Moreover, we let $u(t)$ be unbounded as this choice does not lead to any convergence issues.

Algorithm 1 Gradient Descent

1: **Input**: $h^d(t,x), \lambda, \Delta, n, T$ ▷ Δ:= Step size, n:= Number of iterations
2: **Initialize** $h(t=0,x), p_1(t=T,x), u_0(t)$ ▷ $u_0(t)$:=Initial guess for the control law
3: Solve for $h(t,x)$ in (2)-(7), with (5) set to $u_0(t)$.
4: Compute the initial cost L_0 (8) with $h(t,x)$, $u_0(t)$
5: **for** $i = 1 : n$ **do**
6: Solve for p_1 in (11)-(15), with $\bar{h}(t,x)$ set to $h(t,x)$.
7: Set $p_2(t) = p_1(t, x = 0)$ (see (32))
8: Compute $u_c(t) = u_{i-1}(t) - \Delta(\lambda u_{i-1}(t) + p_2(t))$.
9: **if** $u_c(t_j) < 0$ for some $t_j \in [0,T]$ **then** ▷ Projected Gradient
10: Set $u_c(t_j) = 0$
11: **end if**
12: Solve for $h_c(t,x)$ in (2)-(6), with (5) set to $u_c(t)$
13: Compute cost L_i with $h_c(t,x)$, $u_c(t)$
14: **if** $L_i < L_{i-1}$ **then**
15: $u_i(t) = u_c(t)$
16: $h(t,x) = h_c(t,x)$
17: **else**
18: Set $\Delta = \Delta/2$
19: **end if**
20: **end for**

3. Numerical studies

To simulate the thin-film equation (2) and its adjoint equation (11) with their respective boundary conditions, (5)–(6), (12)–(15), we use finite-difference method for space discretization. In particular, we choose a uniform grid and finite-difference of second-order of accuracy. This results in a N-dimension ordinary differential equation (ODE) in time. The ODE obtained is simulated in *Matlab*, using the *ode15s* solver, a variable-step, variable-order solver based on the numerical differentiation formulas (NDFs) of orders 1 to 5. The necessity of this solver arises due to the stiffness of the system.

We test the optimal control design in two settings: in Section 3.1, the desired profile h^d is set to be a constant function, and in Section 3.2, h^d is set to be a traveling wave of given speed. In the examples presented next, we make the following choices of initial conditions and parameters. The initial condition for the forward Eq. (2) is set to be a near constant function h_0 such that the integral of h_0 over $[0, L]$ is close to the integral of h^d. If the initial condition h_0 is not chosen in this way, the optimization algorithm may fail to converge to a solution. This may be due to the infeasibility of the resulting optimization problem when the initial condition of the PDE is far away from the desired configuration. In such a situation, we say that the control system is not *globally controllable*. The control is initialized to be a strictly positive constant function u_0. The weighting parameter λ in (8) is set to be 1. We choose the values of u_0, final time T, and step size Δ specific to the example, and presented within each case.

3.1. Spatially-uniform solutions

We begin by discussing the stability of spatially-uniform profiles for (2) under periodic boundary conditions. Although these results do not apply to the boundary conditions that we consider (5)–(6), we expect them to hold for the subdomain away from the inlet and outlet boundaries at $x = 0, L$. Consider a spatially-uniform film $h(t, x) = \tilde{h}$, over a periodic domain $[0, l]$, perturbed by an infinitesimal Fourier mode,

$$h = \tilde{h} + \epsilon e^{\mathrm{i}(kx - \Lambda t)}. \tag{19}$$

Here, $k = 2\pi\hat{k}/l$ is the wave number, $\hat{k} = 1, 2, \ldots$ represents the number of waves in the perturbation, Λ is the wave frequency, and $\epsilon \ll 1$ is the initial amplitude. Substituting this expression into (2) and linearizing around the base state $\tilde{h}$ yields the dispersion relation,

$$\Lambda = 3G\tilde{h}k + \mathrm{i}\tilde{h}^3k^2(1 - k^2), \tag{20}$$

where $c = 3G\tilde{h}$ is the speed of linear kinematic wave solutions of (2) for small wave numbers. The form (20) indicates that the second-order azimuthal curvature term $(h^3h_x)_x$ is destabilizing, and the fourth-order streamwise surface tension $(h^3h_{xxx})_x$ term is stabilizing. When the effective growth rate $\mathrm{Im}(\Lambda)$ is greater than 0, the spatial perturbation grows in time and the flat film $\tilde{h}$ becomes long-wave unstable with respect to any wave number $0 < k < 1$. Alternatively, choosing $\hat{k} = 1$ in (20) shows that the flat film is linearly unstable for any domain size $l > 2\pi$.

Next, we consider the steady state solution $\tilde{h}(x)$ of the model (2) subject to the inlet and outlet boundary conditions (5)–(6). By setting the time derivative term $h_t = 0$ in (2) and integrating once, we obtain the third-order ODE for the steady state solution $\tilde{h}(x)$,

$$\frac{d^3\tilde{h}}{dx^3} + \frac{d\tilde{h}}{dx} = \frac{u}{\tilde{h}^3} - G, \tag{21}$$

subject to the boundary conditions

$$\tilde{h}(0) = h_{in}, \quad \tilde{h}_x(L) = \tilde{h}_{xxx}(L) = 0. \tag{22}$$

In the absence of active control, we assume that the boundary control is constant in time, $u(t) \equiv u_0$. This ODE is similar to the one studied in [34] that models the meniscus structure of a surface-tension driven liquid films. Since $\tilde{h}(x)$ satisfies the boundary conditions $\tilde{h}_x(L) = \tilde{h}_{xxx}(L) = 0$, (21) yields the relation $\tilde{h}(L) = (u_0/G)^{1/3}$. Therefore, the steady-state flat film solution $\tilde{h} \equiv h_{in}$ of (2) only exists if the control u_0 satisfies $u_0 = h_{in}^3G$. A non-trivial steady state solution for the boundary value problem (21)–(22) is determined by the Bond number G, the inlet film thickness h_{in}, and the flux u_0. By setting the derivative terms $d^3\tilde{h}/dx^3 = d\tilde{h}/dx = 0$ in (21), the asymptotic behavior of a typical nontrivial steady state satisfies

$$\tilde{h} \to (u_0/G)^{1/3} \quad \text{for } x \to L. \tag{23}$$

Alternatively, to obtain a steady state solution of a desired flat film thickness $h \to h^d$ away from the inlet, the boundary flux control u_0 should satisfy

$$u_0 \sim G(h^d)^3. \tag{24}$$

3.1.1. Example 1

In view of the discussion above, we consider the optimal control Problem 2.1 with a spatially constant desired profile on a domain of length $L > 2\pi$. Specifically, we consider a desired profile $h^d(t, x) = 0.5$ on a domain of size $L = 50$ with the Bond number $G = 0.5$. The Rayleigh–Plateau instability dominates the system due to the input flux, the relatively long domain, and low Bond number, causing the uniform film to break into ripples. This spatial instability is numerically shown in the simulation of the uncontrolled system (2) in Fig. 1(a). Starting from a spatially-uniform initial condition $h_0 = 0.5$ in (7), the sequential plots of $h(t, x)$ in Fig. 1(a) show the evolution of the PDE solution to the uncontrolled system (2), where the input flux (5) is set to a (time-invariant) constant function $u = u_0 \equiv 0.5$. Driven by the Rayleigh–Plateau instability, the solution develops a wavy pattern away from the inlet.

We apply the optimal control Algorithm 1 to this example for final time $T = 500$. Identical initial condition $h_0 = 0.5$ is used for the forward equation similar to the uncontrolled case. Fig. 1(b) shows the simulation of the forward Eq. (2) under the boundary control $u(t)$ (5) obtained from the algorithm. The control u in time is shown in Fig. 1(c). We observe that the controlled system does not break into ripples and converges to approximately $h \approx 0.47$ away from the inlet, close to the desired flat film $h^d = 0.5$. Numerical simulation suggests that the observed trend of h, which forms a meniscus like profile starting from 0.5 and converges to 0.47, is locally stable. The optimal control algorithm appears to converge to this nontrivial equilibrium. Moreover, we observe that the average value of u is 0.05, which is close to $u_0 \sim 0.0625$ predicted by the formula (24) for $G = 0.5$ and $h^d \equiv 0.5$. The Rayleigh–Plateau instability is not expected to dominate under this low average value of input flux $u_0 \sim 0.05$. However, this example shows that the optimal control algorithm produces an output that can be verified against the analytical result obtained in (24). Moreover, the need to design such control laws will be better appreciated in the upcoming sections, where we will consider traveling waves as the desired film profile.

3.2. Traveling wave solutions

In this section, we choose h^d to be a traveling wave of desired characteristics. We generate these traveling waves by considering (2) over a periodic domain $x \in [0, L]$ with boundary conditions $h^d(t, x) = h^d(t, x + L)$. The PDE has traveling wave solutions that take the form,

$$h^d(t, x) = H(\xi), \qquad \xi = x - ct, \tag{25}$$

where c is the speed of the traveling wave. Substituting the ansatz (25) into (2) yields a fourth-order nonlinear ordinary differential equation for $H(\xi)$,

$$-cH_\xi + \left[H^3\left(G + H_\xi + H_{\xi\xi\xi}\right)\right]_\xi = 0. \tag{26}$$

This is a nonlinear eigenvalue problem for the traveling wave profile H and the speed c. We apply Newton's method to solve Eq. (26), where c is treated as an unknown. Following the numerical method used in [2], we impose a constraint on mass conservation as follows. To achieve local uniqueness of the solution, define

$$M_0 = \int_0^L H(\xi)\, d\xi, \tag{27}$$

and set $H(\xi_0) = H_0$, for some $0 \le \xi_0 \le L$. Applying the *numerical continuation method* to the system yields a family of traveling wave solutions $H(\xi; M_0, L)$ of (26) and (27), parameterized by paired parameters (M_0, L).

We note that the traveling waves $H(\xi)$ do not necessarily satisfy the boundary conditions (5)–(6). In fact, for liquid flowing down a vertical cylindrical fibers, the dynamics of the flow near the inlet and outlet strongly depend on the boundary conditions [1]. For droplet dynamics in the Rayleigh–Plateau regime where a steady train of droplets travel down the fiber with nearly constant speed and spacing, one may approximate the flow dynamics away from the inlet and outlet by traveling waves [2]. In this work, we will use traveling wave solutions $H(\xi)$ associated with periodic boundary conditions as desired solution profiles in the control problem.

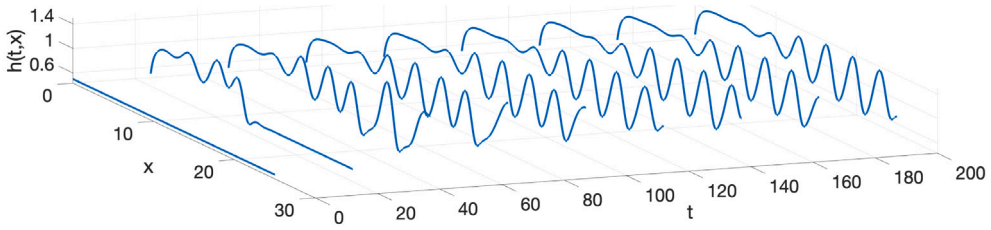

(a) Simulation of uncontrolled $h(t,x)$, with $u_0 = 0.5$

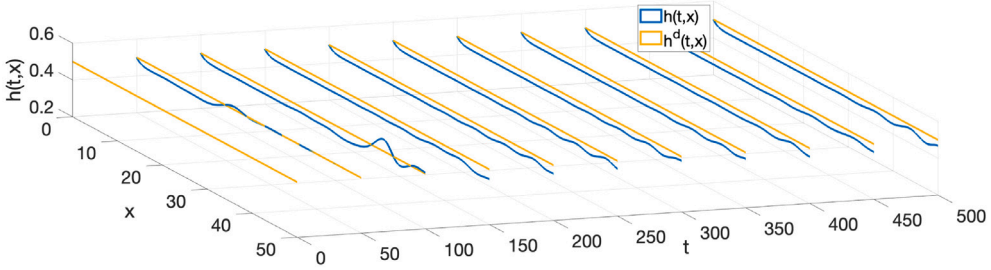

(b) Simulation of controlled $h(t,x)$ against the desired traveling wave profile $h^d = 0.5$

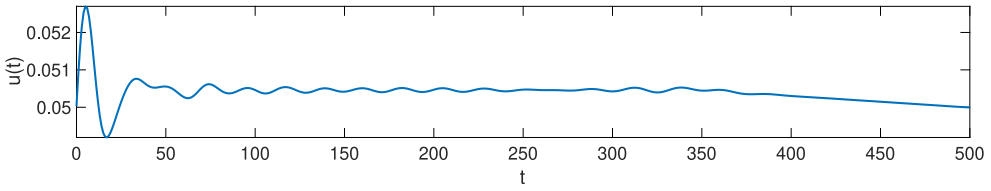

(c) Corresponding $u(t)$ obtained from the optimal control algorithm

Fig. 1. Simulation from Example 1 on a domain size $L = 50$, with $G = 0.5$ and $h_0 = 0.5$.

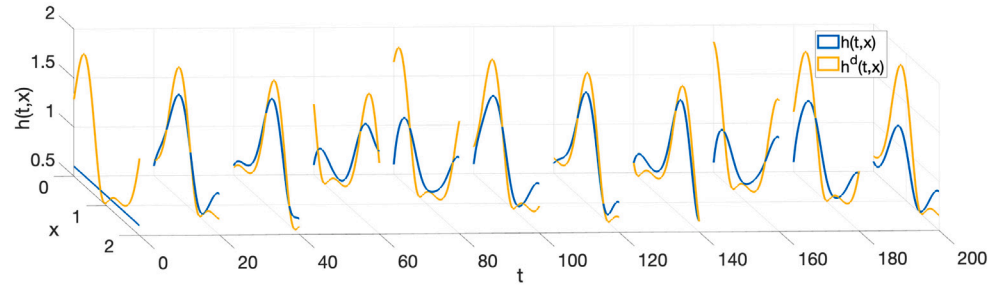

(a) Simulation of controlled $h(t,x)$ against the desired traveling wave profile $h^d(t,x)$.

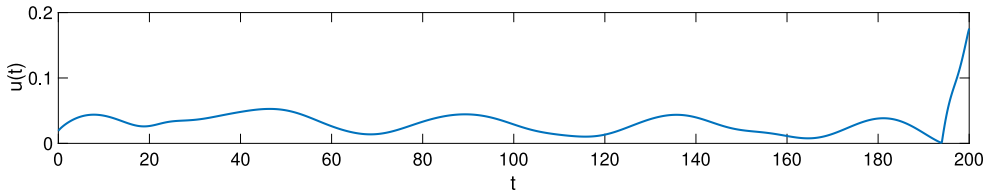

(b) Corresponding $u(t)$ obtained from the optimal control algorithm.

Fig. 2. Simulation from Example 2 on domain size $L = 10$, with $G = 0.5$ and $M_0 = 3.622$.

3.2.1. Example 2: Slow traveling waves

As a first example, we numerically generate a relatively 'slow' traveling wave $H(\xi)$ over a periodic domain of size $L = 10$ by solving the traveling wave ODE (26) subject to the constraint (27) with mass $M_0 = 3.622$ and Bond number $G = 0.5$. The generated traveling wave is associated with a relatively slow speed $c = 0.2$, and its evolution in time $h^d(t,x) = H(x - ct)$ is shown in orange in Fig. 2(a). We verify numerically that the one-period traveling wave $H(\xi)$ is stable over the domain $0 \le \xi \le L$ with respect to perturbations of the same period. A detailed stability analysis of traveling waves in similar thin film models can be found in [2].

We choose the initial condition for the forward Eq. (2) to be the constant function $h_0 = 0.4$. The optimal control algorithm was run for $T = 200$, which corresponds to 4 cycles of the wave traveling

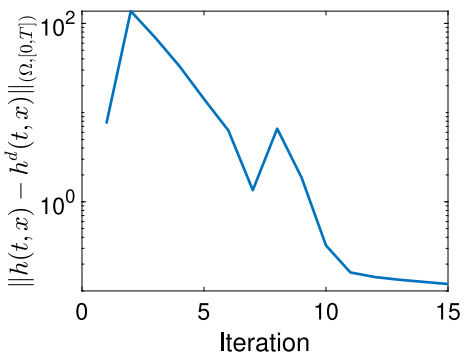

Fig. 3. Logarithm of the cost function (8), with $\lambda = 0$, evaluated in Example 2, corresponding to Fig. 2(a), against iterations.

over the domain $[0, L]$. The boundary control function $u(t)$ obtained from the algorithm is presented in Fig. 2(b). As expected, we observe that the control u shows periodicity; moreover, it appears to achieve a steady state type of behavior away from $t = T$. We simulate the solution of (2) after substituting the u obtained from the algorithm in (5). Fig. 2(a) shows the snapshots of time and spatial evolution of the solution $h(t, x)$. Fig. 3 shows the $L^2([0, T], \Omega)$ error between h and h^d against the number of iterations. We observe that the film thickness h indeed converges approximately to h^d. In general, on short domains, the fluid film converges to a uniform film, but this example shows that active control can be used to make the fluid film break into ripples.

To test our algorithm on long domains, we duplicate the desired traveling wave h^d (shown in Fig. 2(a)) over multiples of $L = 10$. For example, duplicating over $L = 40$ produces a train of 4 droplets, while duplicating over $L = 50$ produces a train of 5 droplets. Both are shown in red at an arbitrary time instant t in Figs. 4(a) and 4(b), respectively. Our numerical study shows that these periodic multi-pulse traveling waves are unstable under periodic boundary conditions. Perturbing these multi-pulse traveling waves over the periodic domain $0 \le x \le L$ leads the dynamic solution to the PDE (2) produce irregular wavy patterns in long-time simulations. However, using the optimal control algorithm, we are able to design a boundary control that generates consistent PDE solutions that resemble the desired traveling waves. In the former case, i.e. $L = 40$, the algorithm was run for $T = 200$. In the latter case, $L = 50$, the final time was set at $T = 300$. In both cases, the initial condition of the forward equation is set at $h_0 = 0.4$. Figs. 4(a) and 4(b) show snapshots of the space evolution of the controlled h at $t = 180$ and $t = 260$, respectively. We observe that in both these cases, the optimal control algorithm is able to find a u that drives the system (2) close to the desired wave profile h^d, away from the boundary.

3.2.2. Example 3: Fast traveling waves

For this example, we generate a 'fast' traveling wave on $L = 10$ by solving (26) over a periodic domain with $M_0 = 10.088$ and $G = 0.5$. The traveling wave obtained has a speed $c = 1.652$, and its evolution in time is shown in orange in Fig. 5(a). The initial condition of the forward Eq. (7) is set at $h_0 = 0.6$. The optimal control $u(t)$ generated in this case, obtained for $T = 200$, is presented in 5(b).

Fig. 6 shows the $L^2([0, T], \Omega)$ error between $h(t, x)$ and $h^d(t, x)$. Here we observe that the error is significantly higher than in Example 2. This can also be noted from the h simulation in Fig. 5(a), we observe that although the controlled h is able to match h^d in frequency, it fails to do so in amplitude. We believe that this is because in Example 2 the wave speed, $c = 0.2$, is slower than this example's wave speed, $c = 1.652$. There appears to be a limitation on the speed of the traveling wave that prohibits reaching this solution h^d exactly. This indicates that the set of reachable states from a given initial condition does not necessarily include all film profiles.

Furthermore, we extend the domain from $L = 10$ to 40 and duplicate the h^d profile from Fig. 5(a) to obtain a train of 4 pulses. Similar to Example 2 discussed in Section 3.2, the single pulse traveling wave $h^d(\xi)$ considered in this example is stable over a periodic domain, while the 4-pulse traveling wave is unstable. The simulated controlled $h(t, x)$ is shown in Fig. 7 at time instant $t = 54$. However, in this case, we observe that the algorithm is not able to find a control u that makes the system converge to h^d. This is unlike in Example 2 where an optimal control is found for longer domains. This could be attributed to the higher speed of the traveling wave. Without a controllability analysis, it appears that the algorithm works better for slow traveling waves or over shorter domains.

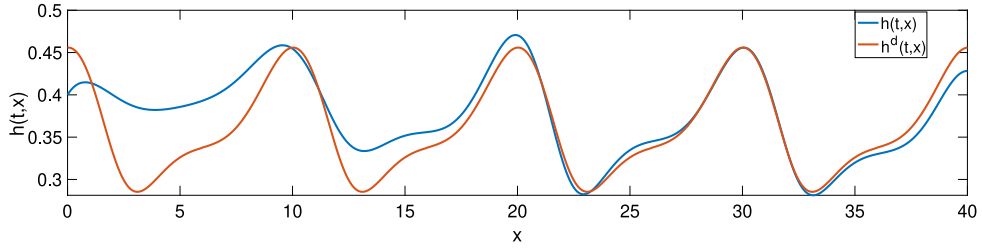

(a) Snapshot at $t = 180$, over $L = 40$

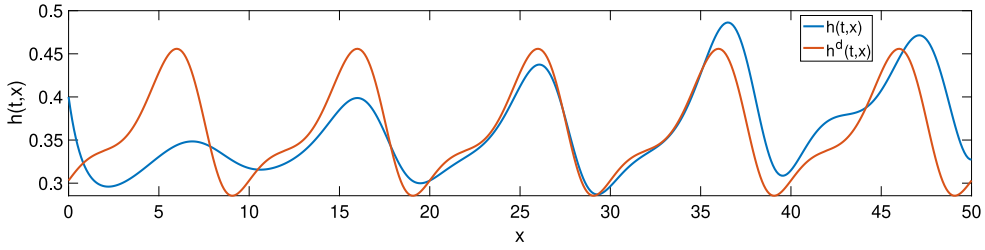

(b) Snapshot at $t = 260$, over $L = 50$

Fig. 4. Simulation of the controlled $h(t, x)$ against the desired traveling wave profile $h^d(t, x)$ at specific time instants t, over different domain sizes L, with $G = 0.5$. The profile h^d in each case is obtained by replicating the h^d from Example 2 (shown in Fig. 2(a)) over L.

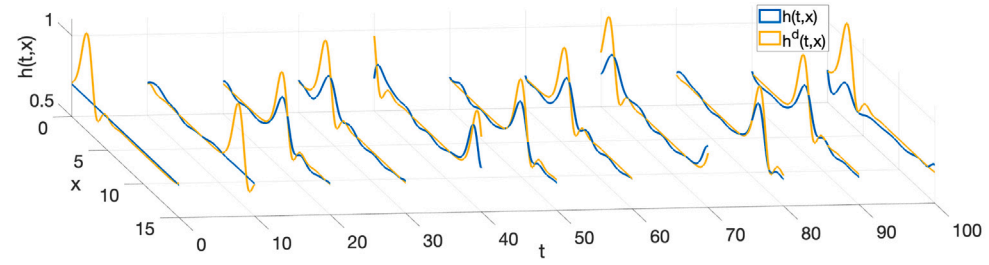

(a) Simulation of controlled $h(t,x)$ against the desired traveling wave profile $h^d(t,x)$.

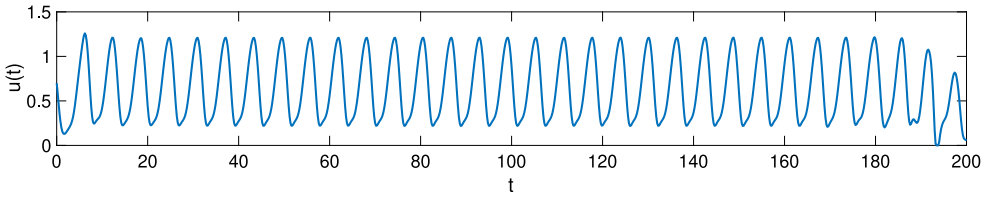

(b) Corresponding $u(t)$ obtained from the optimal control algorithm.

Fig. 5. Simulation from Example 3 on domain size $L = 10$, with $G = 0.5$ and $M_0 = 10.088$.

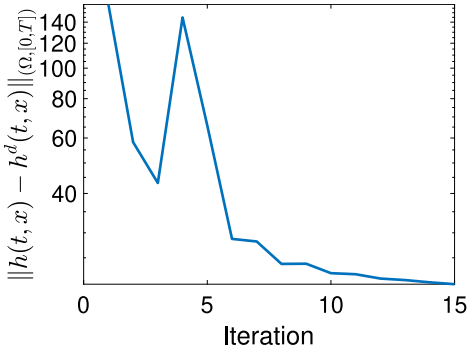

Fig. 6. Logarithm of the cost function (8), with $\lambda = 0$, evaluated in Example 3 corresponding to 5(a), against iterations.

3.2.3. Example 4: Isolated pulse with large inter-pulse spacing

As our final example, we generate a traveling wave $h^d(t,x)$ that has a higher speed on a long domain, as compared to Example 3. Similar to the previous cases, we generate h^d by solving the traveling wave ODE (26) under periodic boundary conditions on $L = 30$ with $M_0 = 22$ and Bond number $G = 1$. This results in an unstable traveling wave of speed $c = 2.13$. PDE simulation of Eq. (2) starting from this isolated pulse with a small perturbation yields a transition into a train of two-pulse traveling wave over the periodic domain. Snapshots of the spatial evolution of desired wave profile are shown in orange in Fig. 8(a). The optimal control found in this case is presented in Fig. 8(b). Snapshots of the corresponding solution $h(t,x)$ are presented in Fig. 8(a). Although we expect that under this large Bond number $G = 1$ and over a relatively short domain of size $L = 30$, the fluid film will converge to a uniform film away from the inlet, with active control, the system is able to track the desired traveling wave closely.

Similar to the previous cases, we duplicated h^d, presented in 8(a), to obtain two pulses over $L = 60$. Fig. 9 shows the simulation of the controlled h at a time step $t = 170$. We observe that, despite the much higher speed in this case, the system is able to track h^d very closely, unlike in the case shown in Fig. 7. We believe this could be attributed to the fact that in this case, the frequency of h^d, due to higher inter-pulse spacing, is smaller than the case in 7.

4. Conclusion

Our goal in this work is to present a proof-of-concept that the nonlinear thin-film equation, considered in this paper, can be controlled to both constant and traveling wave profiles of small wave speeds, over short domain sizes. Specifically, with respect to the uniform film profile case, we are able to design (time-dependent) control laws such that the controlled system converges to a uniform film on a domain size where the Rayleigh–Plateau instability is not very significant. With regards to general traveling waves, the controlled system is able to converge to a slow traveling wave on relatively long domain of size up to $L = 50$. For relatively fast traveling waves of high frequency on short domains, the optimal control algorithm generates a control function that matches the traveling wave in frequency, and not in amplitude. However, the algorithm does generate a control law that is able to track fast traveling waves of low frequency on long domains closely. In conclusion, the numerical experiments seem to indicate that the

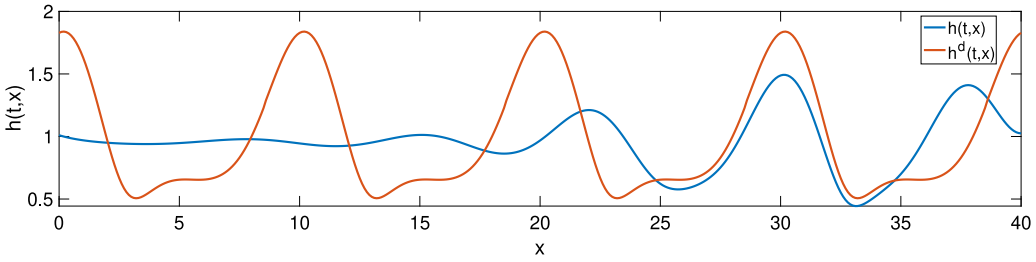

Fig. 7. Simulation of the controlled $h(t,x)$ against the desired traveling wave profile $h^d(t,x)$ at specific time instant $t = 54$, over $L = 40$, with $G = 0.5$. The profile h^d in is obtained by replicating the h^d from Example 3 (shown in Fig. 5(a)) over L.

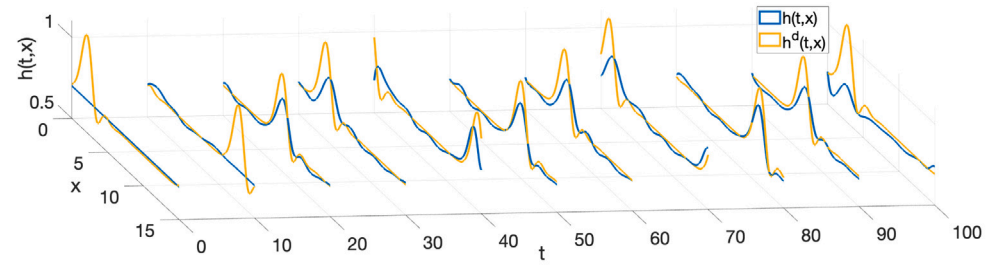

(a) Simulation of controlled $h(t,x)$ against the desired traveling wave profile $h^d(t,x)$.

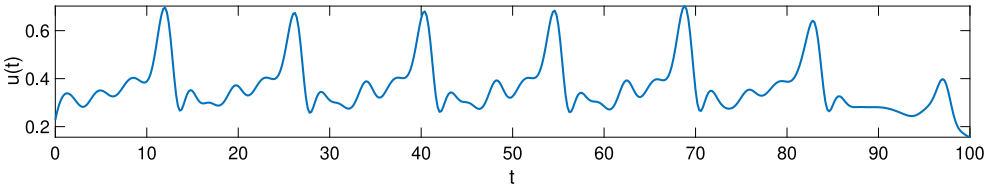

(b) Corresponding $u(t)$ obtained from the optimal control algorithm.

Fig. 8. Simulation from Example 4 on domain size $L = 30$, with $G = 1$ and $M_0 = 22$.

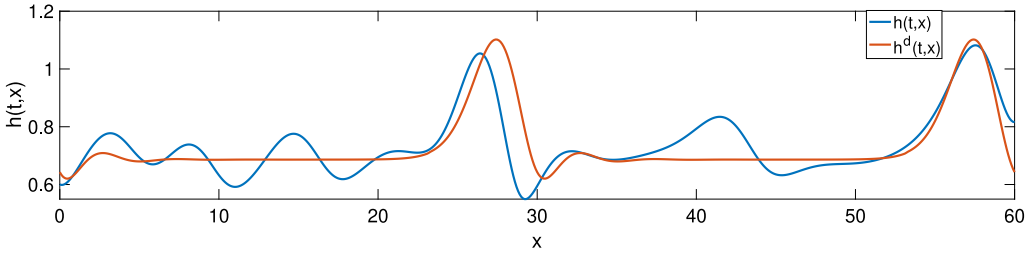

Fig. 9. Simulation of the controlled $h(t,x)$ against the desired traveling wave profile $h^d(t,x)$ at specific time instant $t = 170$, over $L = 60$, with $G = 1$. The profile h^d in is obtained by replicating the h^d from Example 3 (shown in Fig. 8(a)) over L.

thin-film equation under the given boundary conditions is controllable for certain domain sizes, and for initial conditions h_{in}, that are close to h^d in the $L^2(\cdot)$ sense. Our study also highlights the limitations of boundary control. Future work will investigate the possibility of numerically characterizing the controllability properties of the system and designing stabilizing feedback controllers. A stabilizing control law can potentially render a desired film profile locally asymptotically stable.

Declaration of competing interest

The authors declare that they have no known competing financial interests or personal relationships that could have appeared to influence the work reported in this paper.

Data availability

The MATLAB code and data is publicly available at https://github.com/ShibaBiswal/Optimal-Boundary-Control-for-Thin-Film-Equation-

Appendix

We provide the derivation of the adjoint equation in this section. Expanding the LHS of (10), we obtain the following

$$
\begin{aligned}
D_h\mathcal{L}(\bar{h},\bar{u},\bar{p}_i)v = &\int_0^T\int_\Omega (\bar{h}-h^d)v \\
&- \int_0^T\int_\Omega p_1\left\{v_t + \left(3\bar{h}^2v + (3\bar{h}^2\bar{h}_x v + \bar{h}^3 v_x) + (3\bar{h}^2\bar{h}_{xxx}v + \bar{h}^3 v_{xxx})\right)_x\right\} \\
&- \int_0^T p_2\{\left(3\bar{h}^2v + (3\bar{h}^2\bar{h}_x v + \bar{h}^3 v_x) + (3\bar{h}^2\bar{h}_{xxx}v + \bar{h}^3 v_{xxx})\right)\Big|_{x=0} - u\} \\
&- \int_0^T p_3 v(0,t) - \int_0^T p_4 v_x(L,t) - \int_0^T p_5 v_{xxx}(L,t)
\end{aligned}
$$

Applying integration by parts yields:

$$
\begin{aligned}
D_h\mathcal{L}(\bar{h},\bar{u},\bar{p}_i)v = &\int_0^T\int_\Omega (\bar{h}-h^d)v - \int_\Omega (p_1 v)\Big|_0^T + \int_0^T\int_\Omega (p_1)_t v \\
&- \int_0^T (p_1 3\bar{h}^2 v)\Big|_{\partial\Omega} + \int_0^T\int_\Omega (p_1)_x(3\bar{h}^2 v) \\
&- \int_0^T (p_1(3\bar{h}^2\bar{h}_x v + \bar{h}^3 v_x))\Big|_{\partial\Omega} + \int_0^T\int_\Omega (p_1)_x(3\bar{h}^2\bar{h}_x v + \bar{h}^3 v_x) \\
&- \int_0^T (p_1(3\bar{h}^2\bar{h}_{xxx}v + \bar{h}^3 v_{xxx}))\Big|_{\partial\Omega} + \int_0^T\int_\Omega (p_1)_x(3\bar{h}^2\bar{h}_{xxx}v + \bar{h}^3 v_{xxx}) \\
&- \int_0^T p_2\{\left(3\bar{h}^2v + (3\bar{h}^2\bar{h}_x v + \bar{h}^3 v_x) + (3\bar{h}^2\bar{h}_{xxx}v + \bar{h}^3 v_{xxx})\right)\Big|_{x=0} - u\} \\
&- \int_0^T p_3 v(0,t) - \int_0^T p_4 v_x(L,t) - \int_0^T p_5 v_{xxx}(L,t).
\end{aligned}
$$

Applying integration by parts once more yields:

$$
\begin{aligned}
D_h\mathcal{L}(\bar{h},\bar{u},\bar{p}_i)v = &\int_0^T\int_\Omega (\bar{h}-h^d)v - \int_\Omega (p_1 v)\Big|_0^T + \int_0^T\int_\Omega (p_1)_t v \\
&- \int_0^T p_1(3\bar{h}^2 v)\Big|_{\partial\Omega} + \int_0^T\int_\Omega (p_1)_x(3\bar{h}^2 v) - \int_0^T (p_1(3\bar{h}^2\bar{h}_x v + \bar{h}^3 v_x))\Big|_{\partial\Omega} \\
&+ \int_0^T\int_\Omega (p_1)_x(3\bar{h}^2\bar{h}_x v) + \int_0^T ((p_1)_x\bar{h}^3 v)\Big|_{\partial\Omega} - \int_0^T\int_\Omega \left((p_1)_x\bar{h}^3\right)_x v \\
&- \int_0^T (p_1(3\bar{h}^2\bar{h}_{xxx}v + \bar{h}^3 v_{xxx}))\Big|_{\partial\Omega} + \int_0^T\int_\Omega (p_1)_x(3\bar{h}^2\bar{h}_{xxx}v)
\end{aligned}
$$

$$+\int_0^T \left((p_1)_x\bar{h}^3 v_{xx}\right)\Big|_{\partial\Omega} - \int_0^T \left(\left((p_1)_x\bar{h}^3\right)_x v_x\right)\Big|_{\partial\Omega}$$
$$+\int_0^T \left(\left((p_1)_x\bar{h}^3\right)_{xx} v\right)\Big|_{\partial\Omega}$$
$$-\int_0^T \int_\Omega \left((p_1)_x\bar{h}^3\right)_{xxx} v$$
$$-\int_0^T p_2(t)\{\left(3\bar{h}^2 v + (3\bar{h}^2\bar{h}_x v + \bar{h}^3 v_x) + (3\bar{h}^2\bar{h}_{xxx}v + \bar{h}^3 v_{xxx})\right)\Big|_{x=0} - u\}$$
$$-\int_0^T p_3(t)v(0,t) - \int_0^T p_4(t)v_x(L,t) - \int_0^T p_5(t)v_{xxx}(L,t).$$

Since $D_h\mathcal{L}(\bar{h},\bar{u},\bar{p}_i)v = 0$ for all perturbations v, choose a subset of v such that $v = v_x = v_{xx} = v_{xxx} = v_{xxxx} = 0$ at $x = 0, L$, and $v = 0$ at $t = 0, T$. Then $D_h\mathcal{L}(\bar{h},\bar{u},p)v = 0$ implies:

$$D_h\mathcal{L}(\bar{h},\bar{u},p)v = \int_0^T\int_\Omega(\bar{h}-h^d)v + \int_0^T\int_\Omega(p_1)_t v + \int_0^T\int_\Omega(p_1)_x(3\bar{h}^2 v)$$
$$+\int_0^T\int_\Omega(p_1)_x(3\bar{h}^2\bar{h}_x v) - \int_0^T\int_\Omega\left((p_1)_x\bar{h}^3\right)_x v$$
$$+\int_0^T\int_\Omega(p_1)_x(3\bar{h}^2\bar{h}_{xxx}v) - \int_0^T\int_\Omega\left((p_1)_x\bar{h}^3\right)_{xxx} v = 0.$$

Rearranging the terms gives us:

$$(p_1)_t + (\bar{h}-h^d) + 3(p_1)_x\bar{h}^2 + 3(p_1)_x\bar{h}^2\bar{h}_x - \left((p_1)_x\bar{h}^3\right)_x$$
$$+ 3(p_1)_x\bar{h}^2\bar{h}_{xxx} - \left((p_1)_x\bar{h}^3\right)_{xxx} = 0.$$

The equation above can be rewritten to obtain the adjoint Eq. (11).

Next, choose v such that $v_x = v_{xx} = v_{xxx} = v_{xxxx} = 0$ at $x = 0$, and $v = 0$ at $t = 0, T$ and $x = L$, then $D_h\mathcal{L}(\bar{h},\bar{u},\bar{p}_i)v = 0$ implies that,

$$-\int_0^T p_1 3\bar{h}^2 v\Big|_{x=0} - \int_0^T (p_1 3\bar{h}^2\bar{h}_x v)\Big|_{x=0} + \int_0^T ((p_1)_x\bar{h}^3 v)\Big|_{x=0}$$
$$-\int_0^T (p_1 3\bar{h}^2\bar{h}_{xxx}v)\Big|_{x=0} + \int_0^T \left(\left((p_1)_x\bar{h}^3\right)_{xx} v\right)\Big|_{x=0}$$
$$-\int_0^T p_2(t)\left(3\bar{h}^2 v + 3\bar{h}^2\bar{h}_x v + 3\bar{h}^2\bar{h}_{xxx}v\right)\Big|_{x=0} - \int_0^T p_3 v(0,t) = 0.$$

This further implies that,

$$\left(-p_1(3\bar{h}^2)(1+\bar{h}_x+\bar{h}_{xxx}) + (p_1)_x\bar{h}^3 + ((p_1)_x\bar{h}^3)_{xx}\right.$$
$$\left. - p_2(3\bar{h}^2)(1+\bar{h}_x+\bar{h}_{xxx})\right)\Big|_{x=0} = p_3. \tag{28}$$

Proceeding similarly, choose v such that $v_x = v_{xx} = v_{xxx} = v_{xxxx} = 0$ at $x = L$, and $v = 0$ at $t = 0, T$ and $x = 0$, then $D_h\mathcal{L}(\bar{h},\bar{u},\bar{p}_i)v = 0$ implies that,

$$\left(-p_1(3\bar{h}^2)(1+\bar{h}_x+\bar{h}_{xxx}) + (p_1)_x\ \bar{h}^3 + ((p_1)_x\bar{h}^3)_{xx}\right)\Big|_{x=L} = 0. \tag{29}$$

Continuing, choose v such that $v = v_{xx} = v_{xxx} = v_{xxxx} = 0$ at $x = 0$, $v_x = 0$ at $x = L$, and $v = 0$ at $t = 0, T$. Then $D_h\mathcal{L}(\bar{h},\bar{u},\bar{p}_i)v = 0$ yields,

$$(-p_1\bar{h}^3 - ((p_1)_x\bar{h}^3)_x - p_2\bar{h}^3)\Big|_{x=0} = 0. \tag{30}$$

Choose v such that $v = v_{xx} = v_{xxx} = vxxxx = 0$ at $x = L$, $v_x = 0$ at $x = 0$, and $v = 0$ at $t = 0, T$. Then $D_h\mathcal{L}(\bar{h},\bar{u},\bar{p}_i)v = 0$ yields,

$$(-p_1\bar{h}^3 - ((p_1)_x\ \bar{h}^3)_x)\Big|_{x=L} = p_4. \tag{31}$$

Choose v such that $v = v_x = v_{xxx} = v_{xxxx} = 0$ at $x = 0$, $v_{xx} = 0$ at $x = L$, and $v = 0$ at $t = 0, T$. Then $D_h\mathcal{L}(\bar{h},\bar{u},\bar{p}_i)v = 0$ yields,

$$(p_1)_x\ \bar{h}^3\Big|_{x=0} = 0.$$

Since we have assumed that $\bar{h} > 0$, the above equation implies that $(p_1)_x\Big|_{(x=0)} = 0$; this gives us the first boundary condition (12) for p_1 at $x = 0$. Choose v such that $v = v_x = v_{xxx} = v_{xxxx} = 0$ at $x = L$, $vxx = 0$ at $x = 0$, and $v = 0$ at $t = 0, T$. Then, $D_h\mathcal{L}(\bar{h},\bar{u},\bar{p}_i)v = 0$ implies,

$$(p_1)_x\ \bar{h}^3\Big|_{x=L} = 0.$$

Since we have assumed that $\bar{h} > 0$, the above equation further implies that $(p_1)_x(t,x)\Big|_{(x=L)} = 0$, which gives us the third boundary condition (14) for p_1 at $x = L$. Choose v such that $v = v_x = v_{xx} = v_{xxxx} = 0$ at $x = 0$, $v_{xxx} = 0$ at $x = L$, and $v = 0$ at $t = 0, T$. Then $D_h\mathcal{L}(\bar{h},\bar{u},\bar{p}_i)v = 0$ implies,

$$(-p_1\bar{h}^3 - p_2\bar{h}^3)\Big|_{x=0} = 0.$$

This equation further implies

$$p_2(t) = -p_1(0,t). \tag{32}$$

Choose v such that $v = v_x = v_{xx} = v_{xxxx} = 0$ at $x = L$, $v_{xxx} = 0$ at $x = 0$, and $v = 0$ at $t = 0, T$. Then $D_h\mathcal{L}(\bar{h},\bar{u},\bar{p}_i)v = 0$ yields an expression for the Lagrange multiplier $p_5(t)$,

$$p_5 = (-p_1\bar{h}^3)\Big|_{x=L}.$$

Finally, choosing v such that $v = 0$ at $t = 0$ yields,

$$(p_1 v)\Big|_{t=T} = 0 \tag{33}$$

which yields the initial condition for the adjoint Eq. (16) $p_1(T,x) = 0$.

Substituting (6), (14) in (29), we get the second boundary condition (15) for the adjoint equation at $x = L$, $\left(-p_1 + (p_1)_{xxx}\right)\Big|_{x=L} = 0$. Similarly, substituting (32) and (12) in (30), gives us the second boundary condition (13) at $x = 0$, $(p_1)_{xx}\Big|_{x=0} = 0$. Substituting (14) in (31), we get an expression for the multiplier $p_4(t)$,

$$p_4 = \left(p_1\bar{h}^3 - (p_1)_{xx}\bar{h}^3\right)\Big|_{x=L}.$$

And finally, the expression for the Lagrange multiplier $p_3(t)$ can be obtained from (28); the expression can be simplified by substituting the boundary conditions (12)–(13).

References

[1] H. Ji, A. Sadeghpour, Y. Ju, A. Bertozzi, Modelling film flows down a fibre influenced by nozzle geometry, J. Fluid Mech. 901 (2020).
[2] H. Ji, C. Falcon, A. Sadeghpour, Z. Zeng, Y.S. Ju, A.L. Bertozzi, Dynamics of thin liquid films on vertical cylindrical fibres, J. Fluid Mech. 865 (2019) 303–327.
[3] C. Duprat, C. Ruyer-Quil, S. Kalliadasis, F. Giorgiutti-Dauphiné, Absolute and convective instabilities of a viscous film flowing down a vertical fiber, Phys. Rev. Lett. 98 (24) (2007) 244502.
[4] A. Sadeghpour, F. Oroumiyeh, Y. Zhu, D.D. Ko, H. Ji, A.L. Bertozzi, Y.S. Ju, Experimental study of a string-based counterflow wet electrostatic precipitator for collection of fine and ultrafine particles, J. Air Waste Manage. Assoc. (2021) 1–15.
[5] Z. Zeng, A. Sadeghpour, Y.S. Ju, A highly effective multi-string humidifier with a low gas stream pressure drop for desalination, Desalination 449 (2019) 92–100.
[6] A. Sadeghpour, Z. Zeng, H. Ji, N.D. Ebrahimi, A. Bertozzi, Y. Ju, Water vapor capturing using an array of traveling liquid beads for desalination and water treatment, Sci. Adv. 5 (4) (2019) eaav7662.
[7] Z. Zeng, A. Sadeghpour, G. Warrier, Y.S. Ju, Experimental study of heat transfer between thin liquid films flowing down a vertical string in the Rayleigh-Plateau instability regime and a counterflowing gas stream, Int. J. Heat Mass Transfer 108 (2017) 830–840.
[8] Z. Zeng, A. Sadeghpour, Y.S. Ju, Thermohydraulic characteristics of a multi-string direct-contact heat exchanger, Int. J. Heat Mass Transfer 126 (2018) 536–544.
[9] Y. Trifonov, et al., Steady-state traveling waves on the surface of a viscous liquid film falling down on vertical wires and tubes, AIChE J. 38 (6) (1992) 821–834.
[10] A. Frenkel, Nonlinear theory of strongly undulating thin films flowing down vertical cylinders, Europhys. Lett. 18 (7) (1992) 583.
[11] H.-C. Chang, E.A. Demekhin, Mechanism for drop formation on a coated vertical fibre, J. Fluid Mech. 380 (1999) 233–255.
[12] S. Kalliadasis, H.-C. Chang, Drop formation during coating of vertical fibres, J. Fluid Mech. 261 (1994) 135–168.
[13] R.V. Craster, O.K. Matar, On viscous beads flowing down a vertical fibre, J. Fluid Mech. 553 (2006) 85–105.
[14] C. Ruyer-Quil, S.P.M.J. Trevelyan, F. Giorgiutti-Dauphiné, C. Duprat, S. Kalliadasis, Film flows down a fiber: Modeling and influence of streamwise viscous diffusion, Eur. Phys. J. Spec. Top. 166 (1) (2009) 89–92.
[15] C. Ruyer-Quil, P. Treveleyan, F. Giorgiutti-Dauphiné, C. Duprat, S. Kalliadasis, Modelling film flows down a fibre, J. Fluid Mech. 603 (2008) 431–462.
[16] Y. Ruan, A. Nadim, L. Duvvoori, M. Chugunova, Liquid films falling down a vertical fiber: modeling, simulations and experiments, Fluids 6 (8) (2021) 281.

[17] D. Halpern, H.-H. Wei, Slip-enhanced drop formation in a liquid falling down a vertical fibre, J. Fluid Mech. 820 (2017) 42–60.
[18] A. Sadeghpour, Z. Zeng, Y.S. Ju, Effects of nozzle geometry on the fluid dynamics of thin liquid films flowing down vertical strings in the Rayleigh-Plateau regime, Langmuir 33 (2017) 6292–6299.
[19] C. Duprat, C. Ruyer-Quil, F. Giorgiutti-Dauphiné, Spatial evolution of a film flowing down a fiber, Phys. Fluids 21 (4) (2009) 042109.
[20] H. Ji, C. Falcon, E. Sedighi, A. Sadeghpour, Y.S. Ju, A.L. Bertozzi, Thermally-driven coalescence in thin liquid film flowing down a fibre, J. Fluid Mech. 916 (2021).
[21] A. Armaou, P.D. Christofides, Feedback control of the Kuramoto–Sivashinsky equation, Physica D 137 (1–2) (2000) 49–61.
[22] P.D. Christofides, A. Armaou, Global stabilization of the Kuramoto–Sivashinsky equation via distributed output feedback control, Systems Control Lett. 39 (4) (2000) 283–294.
[23] C. Lee, H. Tran, Reduced-order-based feedback control of the Kuramoto–Sivashinsky equation, J. Comput. Appl. Math. 173 (1) (2005) 1–19.
[24] R. Katz, E. Fridman, Finite-dimensional control of the Kuramoto-Sivashinsky equation under point measurement and actuation, in: 2020 59th IEEE Conference on Decision and Control (CDC), IEEE, 2020, pp. 4423–4428.
[25] R. Al Jamal, K. Morris, Linearized stability of partial differential equations with application to stabilization of the Kuramoto–Sivashinsky equation, SIAM J. Control Optim. 56 (1) (2018) 120–147.
[26] W.-J. Liu, M. Krstić, Stability enhancement by boundary control in the Kuramoto–Sivashinsky equation, Nonlinear Anal. TMA 43 (4) (2001) 485–507.
[27] J.-M. Coron, Q. Lü, Fredholm transform and local rapid stabilization for a Kuramoto–Sivashinsky equation, J. Differential Equations 259 (8) (2015) 3683–3729.
[28] M. Maghenem, C. Prieur, E. Witrant, Boundary control of the Kuramoto-Sivashinsky equation under intermittent data availability, in: American Control Conference, 2022.
[29] R.J. Tomlin, S.N. Gomes, G.A. Pavliotis, D.T. Papageorgiou, Optimal control of thin liquid films and transverse mode effects, SIAM J. Appl. Dyn. Syst. 18 (1) (2019) 117–149.
[30] M. Klein, A. Prohl, Optimal control for the thin film equation: Convergence of a multi-parameter approach to track state constraints avoiding degeneracies, Comput. Methods Appl. Math. 16 (4) (2016) 685–702.
[31] A.E. Samoilova, A. Nepomnyashchy, Feedback control of Marangoni convection in a thin film heated from below, J. Fluid Mech. 876 (2019) 573–590.
[32] F. Tröltzsch, Optimal Control of Partial Differential Equations: Theory, Methods, and Applications, Vol. 112, American Mathematical Soc., 2010.
[33] S. Boyd, S.P. Boyd, L. Vandenberghe, Convex Optimization, Cambridge University Press, 2004.
[34] A. Münch, P. Evans, Interaction of advancing fronts and meniscus profiles formed by surface-tension-gradient-driven liquid films, SIAM J. Appl. Math. 66 (5) (2006) 1610–1631.